Optical and Quantum Electronics (2022) 54:380
https://doi.org/10.1007/s11082-022-03742-4

Refined modelling of anisotropy influence on the optical gain in Mid-IR quantum cascade lasers

N. Vuković[1] · J. Radovanović[1] · V. Milanović[1]

Received: 23 November 2021 / Accepted: 8 April 2022 / Published online: 25 May 2022

Abstract
We describe an elaborate model for calculation of optical gain in quantum cascade laser (QCL) taking into account that such complex layered quantum-well based structure should be viewed as an anisotropic material in terms of dielectric constant. The layering induced anisotropy leads to substantial modifications of electron-longitudinal (LO) phonon scattering rates owing to the occurrence of additional resonant frequencies for LO phonons, each affecting the totals scattering rate between relevant subbands. This clearly impacts the carrier distribution between the subbands and alters the degree of population inversion in the active region of a QCL, in comparison to the results of an isotropic permittivity model, as illustrated by our numerical example.

Keywords Quantum cascade laser · LO phonon scattering · Anisotropy of dielectric permittivity

1 Introduction

Quantum cascade laser (QCL) represents a leading-edge unipolar device consisting of a carefully designed array of semiconductor quantum wells which give rise to quantized electron states, and thus facilitate a specific series of intersubband transitions within the conduction band (Faist et al. 1994; Harrison and Valavanis 2016). The benefit of the intersubband transitions is that they allow lasing at energies that are much lower than transitions between atomic levels present in traditional lasers. The active region of a QCL incorporates a large number of periodically repeated stages comprised of gain and injection/relaxation regions. The function of a gain region is to provide a sufficient population inversion necessary for the lasing transition, and the purpose of the injection/relaxation region is to depopulate the lower lasing level and to inject electrons in the upper lasing level of the next cascade (Faist 2013; Jirauschek

This article is part of the Topical Collection on Photonics:Current Challenges and Emerging Applications, Guest edited byJelena Radovanovic, Dragan Indjin, Maja Nesic, Nikola Vukovic andMilena Milosevic.

✉ N. Vuković
nvukovic@etf.bg.ac.rs

[1] University of Belgrade, School of Electrical Engineering, Bulevar kralja Aleksandra 73, 11120 Belgrade, Serbia

and Kubis 2014; Williams 2007). When the bias voltage is applied, an electron transported along the growth direction in ideal conditions emits as many photons as the number of periods. The lasing frequency (determined by the energy difference between the upper and lower laser level), and energy alignment (necessary for an efficient injection into the upper laser level and depopulation of the lower level) therefore require careful design of the quantized states in the QCL device (Jirauschek and Kubis 2014; Radovanović et al. 2021; Smiljanić et al. 2014; Wacker 2012). Engineering of the wave functions by solving the Schrödinger-Poisson equation system governs the strength of both the radiative and nonradiative transitions (Ko and Yu 2010; Mueller and Triplett 2016; Waldmueller et al. 2010).

Continuously operating QCLs in the MIR (3.5–20 μm) offer high output powers, narrow linewidth, tunability, compactness, portability, and favorable wavelength range, thus having extensive applications in health care, stand-off detection of chemical, biological, radiological, and nuclear (CBNR) threats (Fuchs et al. 2010; Li et al. 2015; Ostendorf et al. 2016; Sharma and S 2014), telecommunications and broadband spectroscopy (Hugi et al. 2012; Villares et al. 2014; Vitiello et al. 2015). The ability to emit short pulses due to the sub-picosecond relaxation times of the gain and coherence is an object of a detailed scientific investigation (Opačak and Schwarz 2019; Singleton et al. 2019; Vukovic et al. 2017).

In this paper, we introduce an advanced theoretical model for a QCL as an anisotropic material, and we show how our model behaves compared to the isotropic model which is widely used in the literature (Jirauschek and Kubis 2014). The main contribution consists in the inclusion of dielectric constant anisotropy, as it depends on the structural design (layer parameters), that was previously neglected. Longitudinal optical phonon frequency is not considered here to be a constant, but there is dependence on phonon wavevector in the vicinity of the LO phonon modes: one dependence is on the material system and the others on the transition energies of the structure's active region. Our calculations are based on the system of rate-equations, which is solved iteratively to evaluate carrier densities, scattering rates, and finally the optical gain. An interesting recent study (Lyu and Gmachl 2021) considers correction to the effective refractive index and the confinement factor in QCL waveguide modeling due to the effect of the anisotropic optical gain and non-Hermitian properties of the waveguide structure and materials. Their findings confirm the importance of the inclusion of the anisotropic properties in QCL modeling, however, please note that in our paper we have used different approaches and methods. This communication is organized as follows: Sect. 2 provides a detailed description of the model, in Sect. 3 we discuss results of numerical simulations for a QCL active region design chosen from literature, and Sect. 4 concludes the paper with a brief closing summary.

2 Model

The electron inside a QCL is quantized in one *(x)* dimension, while it is pseudo-free in the other two dimensions (*y, z*) according to the effective mass model. The permeability of a semiconductor-based nonmagnetic metamaterial is $\mu = 1$, while the intersubband induced permittivity for the quantum structure unit cell, considering strong anisotropy of optical properties, is represented by the dielectric permittivity tensor that has the following form (Ginzburg and Orenstein 2008):

$$\varepsilon = \begin{bmatrix} \varepsilon_{\perp} & 0 & 0 \\ 0 & \varepsilon_{\|} & 0 \\ 0 & 0 & \varepsilon_{\|} \end{bmatrix} \tag{1}$$

Here $\varepsilon_y = \varepsilon_z = \varepsilon_{\|}$ are the permittivity components along the quantum well planes (perpendicular to the growth direction x):

$$\varepsilon_{\|}(\omega) = \varepsilon_{\infty}\frac{\omega^2 - {\omega_{LO}}^2}{\omega^2 - {\omega_{TO}}^2} = \varepsilon_{\infty} + \frac{{\omega_{p\|}}^2}{{\omega_{0\|}}^2 - \omega^2} \tag{2}$$

where ω_{LO} and ω_{TO} are longitudinal and transversal optical phonon angular frequencies respectively, ε_{∞} and $\varepsilon(0)$ are permittivities at high and low frequencies, $\omega_{0\|} = \omega_{TO} = \sqrt{\varepsilon_{\infty}/\varepsilon(0)}\omega_{LO}$, and $\omega_{p\|} = \varepsilon_{\infty}\sqrt{\frac{1}{\varepsilon_{\infty}} - \frac{1}{\varepsilon(0)}}$. In our previous work (Dubajić et al. 2018; Vuković et al. 2015) we considered $\varepsilon_{\|}$ to be a constant, equal to ε_b-the averaged permittivity of the background material.

Permittivity along the growth axes (x), denoted by $\varepsilon_{\perp}$, is described by the Lorenzian model (Basu 2003; Ginzburg and Orenstein 2008):

$$\varepsilon_{\perp}(\omega) = \varepsilon_{\|} + \frac{2}{L_p}\frac{e^2}{\varepsilon_0\hbar}\sum_{n>m}\left(N_{s,m} - N_{s,n}\right)\frac{\left|x_{mn}\right|^2\omega_{nm}}{\omega_{nm}^2 - \omega^2} \tag{3}$$

where L_p is the length of the unit cell in the x direction, $N_{s,i}$ represents the spatial sheet density of electrons in the i-th subband (total number of electrons in the subband divided by the spatial area of interest), $\omega_{nm} = \frac{(E_n - E_m)}{\hbar} > 0$, when $n > m$, is the resonant transition frequency between states n and m, x_{mn} is the transition matrix element between states n and m, and ω stands for the angular frequency of the input light.

In this paper, we have assumed that longitudinal optical (LO) phonon scattering is the dominant non-radiative transition mechanism in QCLs of interest. Phonon scattering in a crystal is described by the Fröhlich interaction (Jirauschek and Kubis 2014). The phonon spectrum available to a QCL electron for scattering is approximated to be the phonon spectrum of a bulk sample of the material used in the quantum wells, as in (Baird 2009). Nevertheless, the assumption is also made that the bulk crystal has dispersion such that LO photon can be created or destroyed in a transition at the frequency $\widetilde{\omega_{LO}}\,(\vec{\mathrm{q}})$ which depends on the wavevector $\vec{\mathrm{q}}$.

Electric field originating from LO phonons in the QCL active region has an orthogonal and transverse component $\vec{E} = \overrightarrow{E_{\perp}} + \overrightarrow{E_{\|}} = -\nabla\Phi_0 e^{i\vec{q}\vec{r}}$, where $\Phi_0 e^{i\vec{q}\vec{r}}$ is LO phonon potential, and $\vec{q}$ is LO phonon wave vector. From electrostatics we have $\nabla(\varepsilon_{\perp}\overrightarrow{E_{\perp}} + \varepsilon_{\|}\overrightarrow{E_{\|}}) = 0$, which results in the following transcendent equation:

$$\varepsilon_{\perp}\left(\widetilde{\omega_{LO}}\right)q_{\perp}^2 + \varepsilon_{\|}\left(\widetilde{\omega_{LO}}\right)q_{\|}^2 = 0 \tag{4}$$

where $q_{\perp} \equiv q_x$ and ${q_{\|}}^2 = {q_y}^2 + {q_z}^2$.

Normalization condition for LO phonons (Stroscio and Dutta 2001) results in the following expression for Φ_0

$$\Phi_0^2 = \frac{\widetilde{\omega_{LO}}}{2\varepsilon_0 V}\frac{1}{\rho_{\perp}\left(\widetilde{\omega_{LO}}\right)q_{\perp}^2 + \rho_{\|}\left(\widetilde{\omega_{LO}}\right)q_{\|}^2} \tag{5}$$

where we have introduced two new variables:

$$
\begin{aligned}
\rho_{||} &= \frac{\omega_{p||}^2 \widetilde{\omega_{LO}}^2}{\left(\omega_{0||}^2 - \widetilde{\omega_{LO}}^2\right)^2} \\
\rho_{\perp} &= \rho_{||} + \frac{2e^2}{\varepsilon_0 \hbar L_p} \widetilde{\omega_{LO}}^2 \sum_{n>m} \frac{\left(N_{s,m} - N_{s,n}\right) \left|x_{mn}\right|^2 \omega_{nm}}{\left(\omega_{nm}^2 - \widetilde{\omega_{LO}}^2\right)^2}
\end{aligned}
\tag{6}
$$

We apply the Fröhlich Hamiltonian to Fermi's golden rule and calculate the phonon scattering rate. The interaction Hamiltonian between an electron and a LO phonon is given by (Stroscio and Dutta 2001):

$$
\hat{H}' = \sum_{\vec{q}} \Phi_0\left(\vec{q}\right)\left[\hat{a}_q e^{i\vec{q}\vec{r}} + \hat{a}_q^{+} e^{-i\vec{q}\vec{r}}\right] \tag{7}
$$

where $\hat{a}_q^{+}$ and $\hat{a}_q$ are phonon creation and annihilation operators. The interaction Hamiltonian represents a sum of all the possible discreet phonon modes **q**. Since the crystal is large enough the modes are assumed to be infinitesimally close and the sum can be approximated by an integral in a standard way.

Fermi's golden rule can be written for the transition rate $w_{i\to f}^{ems,abs}$ from an initial quantized intersubband state i in the x dimension and initial free state with wave vector $\vec{k}_i$ in the y–z dimension and initial crystal phonon state $N_{i,\vec{q}}$ to a final intersubband state f in the x dimension and final free state with wave vector $\vec{k}_f$ in the y–z dimension and final crystal phonon state $N_{f,\vec{q}}$ (Baird 2009; Harrison and Valavanis 2016):

$$
\begin{aligned}
w_{i\to f}^{ems,\,abs}\left(\vec{k}_i, \vec{k}_f\right) &= \frac{2\pi}{\hbar}\left|H'_{if}\right|^2 \delta\left(E_i\left(\vec{k}_i\right) - E_f\left(\vec{k}_f\right) \mp \hbar\widetilde{\omega_{LO}}\right) \\
&= \frac{2\pi e^2}{\hbar} \sum_{\vec{q}} \left(N_q + \frac{1}{2} \pm \frac{1}{2}\right)\left|M_{if}\right|^2 \Phi_0^2 \delta\left(E_i\left(\vec{k}_i\right) - E_f\left(\vec{k}_f\right) \mp \hbar\widetilde{\omega_{LO}}\right)
\end{aligned}
\tag{8}
$$

where $H'_{if} = <\Psi_f, \vec{k}_f, N_{f,\vec{q}}\left|\hat{H}'\right|\Psi_i, \vec{k}_i, N_{i,\vec{q}}>$. Note that the upper/lower signs in Eq. (8) designate emission/absorption transition. Phonon occupation number is given by Bose–Einstein statistics (Harrison and Valavanis 2016): $N_q = \frac{1}{e^{\hbar\widetilde{\omega_{LO}}/kT} - 1}$. Matrix element M_{if} is defined as:

$$
M_{if} = <\Psi_f(x)\left|e^{\mp i q_\perp x}\right|\Psi_i(x)> \delta(k_{f,y} \pm q_y - k_{i,y})\delta(k_{f,z} \pm q_z - k_{i,z}) \tag{9}
$$

From the conservation of momentum expressed via the Dirac deltas in the Eq. (9), the transverse component of the interaction wavevector ($\vec{q}_{||}$) is just the difference of the initial and final wavevectors, i.e. $\vec{k}_f = \vec{k}_i + \vec{q}_{||}$, which after the application of the cosine theorem gives rise to:

$$
{q_{||}}^2 = {k_i}^2 + {k_f}^2 - 2k_i k_f \cos\theta \tag{10}
$$

To find the transition rate into a specific quantum state f in the x dimension but any final state in the y–z dimensions we need to integrate over all possible final states in the y–z dimension. After some basic mathematical transformations, we arrive at:

$$w_{i\to f}^{ems,\,abs}\left(k_i^2\right)=\frac{me^2}{8\pi^2\hbar^2\varepsilon_0}\int_{q_\perp=-\infty}^{\infty}\int_{\theta=0}^{2\pi}\frac{\widetilde{\omega_{LO}}\left(N_q+\frac{1}{2}\pm\frac{1}{2}\right)}{\rho_{||}q_{||}^2+\rho_\perp q_\perp^2}\left|\left\langle\Psi_f(x)\middle|e^{\mp iq_\perp x}\middle|\Psi_i(x)\right\rangle\right|^2dq_\perp d\theta \tag{11}$$

We have applied the conservation of energy Dirac delta, i.e.

$$k_f{}^2=k_i{}^2+\frac{2m^*}{\hbar^2}(E_i(0)-E_f(0)\mp\hbar\,\tilde{\omega}_{LO}) \tag{12}$$

Finally, averaging over all initial wave vectors results in total scattering rate:

$$\frac{1}{\tau_{if}}=W_{i\to f}^{ems,abs}=\frac{\int_{-\infty}^{\infty}w_{i\to f}^{ems,abs}\left(k_i{}^2\right)f_{FD}(k_i)(1-f_{FD}\left(k_f\right))k_idk_i}{\int\limits_{-\infty}^{\infty}f_{FD}(k_i)dk_i} \tag{13}$$

where we have used Fermi distribution for electrons in a subband:

$$f_{FD}\left(k_i\right)=\frac{1}{1+\exp[(E_i(0)+\hbar^2k_i{}^2/2m^*-E_{F,i})/k_BT]} \tag{14}$$

Fermi energy of the i-th subband depends on the electron sheet density $N_{s,i}$ and electron temperature (set to 300 K in this work) as:

$$E_{F,i}=E_i(0)+k_BTln[\exp\left(\frac{\pi\hbar^2N_{s,i}}{k_BTm^*}\right)-1] \tag{15}$$

The populations are to be determined by solving the system of rate equations which depend on scattering rate calculations, nevertheless, the individual subband Fermi levels are found from the populations and used in the scattering calculations. Since all these properties are circularly dependent they must be found iteratively (self-consistently).

Rate equations for a three-level system in equilibrium (the sum of all possible transition rates into the level and out of the level are equal) that we are considering in this paper are:

$$\begin{aligned}\frac{\mathrm{d}N_3}{\mathrm{d}t}&=\frac{J_{in}}{e}-\frac{N_{s,3}}{\tau_{31}}-\frac{N_{s,3}}{\tau_{32}}+\frac{N_{s,1}}{\tau_{13}}+\frac{N_{s,2}}{\tau_{23}}=0\\ \frac{\mathrm{d}N_2}{\mathrm{d}t}&=\frac{N_{s,3}}{\tau_{32}}+\frac{N_{s,1}}{\tau_{12}}-\frac{N_{s,2}}{\tau_{21}}-\frac{N_{s,2}}{\tau_{23}}=0\\ \frac{\mathrm{d}N_1}{\mathrm{d}t}&=\frac{N_{s,3}}{\tau_{31}}+\frac{N_{s,2}}{\tau_{21}}-\frac{N_{s,1}}{\tau_{13}}-\frac{N_{s,1}}{\tau_{12}}-\frac{J_{\mathrm{out}}}{e}=0\end{aligned} \tag{16}$$

From the conditions of continuity, we have $J_{in}=J_{out}=J$. The sum of the populations of the three subbands is equal to the constant value N_s determined by doping. As for the iterative procedure we need to set some initial values for electron densities, we opt here for equal initial distribution, so that the total electron density is evenly divided among the levels.

3 Anisotropic gain

As a starting point of our analysis, we use the following equation derived from the Maxwell EQs. for a waveguide:

$$\kappa_x^2 + \frac{\varepsilon_{||}}{\varepsilon_{\perp}}\kappa_z^2 = \mathcal{E}_{||}\kappa_0^2 \tag{17}$$

where κ_z is z-component of the photon wavevectorκ, a real quantity, and it can be expressed as: $\kappa_z = |\kappa_R|\sin\theta_\kappa$, where $|\kappa_R|$ denotes the modulus of the real part of the photon wavevectorκ, and θ_κ is the angle between the real part of κ and the growth axes x. The x component of κ is a complex number with a real part $k_{x_R} = |k_R|cos\left(\theta_\kappa\right)$. We have only considered TM polarization in this manuscript since the equation for TE modes is the same as for the case of an isotropic medium where the dielectric permittivity is independent of x (quantum well growth direction). Therefore, the case of TE modes was not interesting for further analysis and was not considered in our work.

We can split Eq. (17) into its real and imaginary parts and introduce new variables a and b:

$$\begin{aligned}\mathrm{Re}\left\{\kappa_x^2\right\} &= \varepsilon_{||}\kappa_0^2 - \varepsilon_{||}\mathrm{Re}\left\{\frac{1}{\varepsilon_{\perp}}\right\}\kappa_z^2 = a \\ \mathrm{Im}\left\{\kappa_x^2\right\} &= -\varepsilon_{||}\mathrm{Im}\left\{\frac{1}{\varepsilon_{\perp}}\right\}\kappa_z^2 = b\end{aligned} \tag{18}$$

which we can use to express real and imaginary parts of κ_x as:

$$\begin{aligned}k_{x_R} &= \sqrt{\frac{a + \sqrt{a^2 + b^2}}{2}}, \\ k_{x_I} &= \frac{b}{2k_{x_R}}\end{aligned} \tag{19}$$

Angle θ_κ is set in advance and phonon wavevector components κ_x and κ_z can be determined as a function of θ_κ.

Quantum cascade laser gain can be expressed as (see Appendix A for more details) as:

$$G_{if} = \frac{e^2\pi n_R L(\hbar\omega)}{m_0^2\omega\varepsilon_0 c\left|\varepsilon_{\perp}\right|^2}\frac{\left|P_{i,f_x}\right|^2 sin^2\left(\theta_\kappa\right) + \frac{\left|\mathcal{E}_{\perp}\right|^2}{\varepsilon_{||}^2}\left|P_{i,f_z}\right|^2\left(cos^2\left(\theta_\kappa\right) + \left|\frac{\kappa_{x_I}}{\kappa_R}\right|^2\right) - 2Re\left\{\frac{\kappa_z P_{i,f_x}\kappa_x{}^* P_{i,f_z}^*}{\left|\kappa_R\right|^2\mathcal{E}_{\perp}\mathcal{E}_{||^*}}\right\}}{\sqrt{\frac{cos^2\left(\theta_\kappa\right)}{\varepsilon_{||}{}^2} + \left[Re\left\{\frac{1}{\varepsilon_{\perp}}\right\}\right]^2 sin^2\left(\theta_\kappa\right)}}\left(N_{s,i} - N_{s,f}\right) \tag{20}$$

In the above Eq. (20) n_R is the real part of the QCL refractive index:

$$n_R^2 = \frac{\left|\kappa_R\right|^2}{\kappa_0^2} = \frac{\kappa_z^2 + \kappa_{x_R}^2}{\frac{\kappa_{x_R}^2}{\varepsilon_{||}} + Re\left\{\frac{1}{\varepsilon_{\perp}}\right\}\kappa_z^2} = \frac{\varepsilon_{||}\left(tg^2\left(\theta_\kappa\right) + 1\right)}{1 + Re\left\{\frac{1}{\varepsilon_{\perp}}\right\}\varepsilon_{||}tg^2\left(\theta_\kappa\right)} \tag{21}$$

$L(\hbar\omega)$ is the Lorentzian; P_{i,f_x} and P_{i,f_z} are form-factors that depend on the total electron wave functions Ψ_i, Ψ_f:

$$\begin{aligned} P_{i,f_x} &= \int \Psi_f^* e^{i(\kappa_x x+\kappa_z z)} \hat{p}_x \Psi_i dV \\ P_{i,f_z} &= \int \Psi_f^* e^{i(\kappa_x x+\kappa_z z)} \hat{p}_z \Psi_i dV \end{aligned} \tag{22}$$

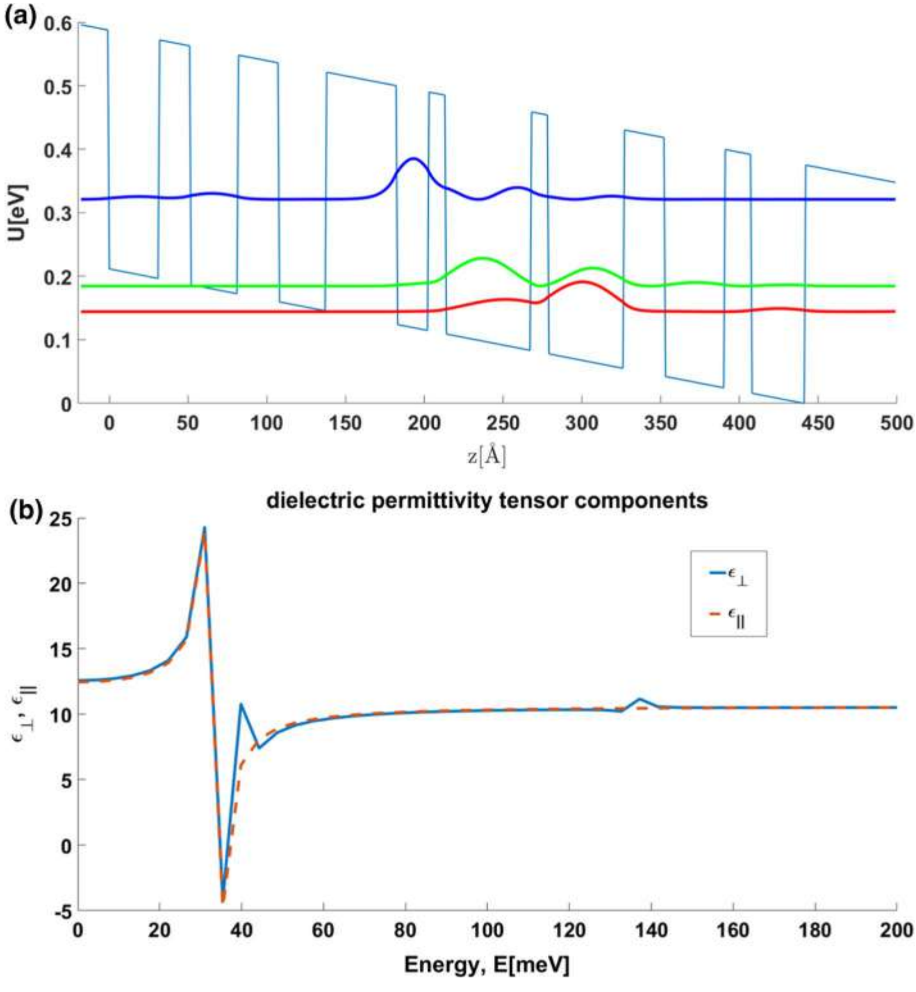

Fig.1 **a** One GaAs/$Al_{0.45}Ga_{0.55}As$ QCL period (cascade) has L_p=46 nm length. Thicknesses of the grown layers shown in Fig starting from the first well on the left are given in nanometers in order: 3.2/2.0/3.0/2.6/3.0/4.5/2.0/1.1/5.4/1.1/4.8/2.6/3.8/1.7/3.4/1.8. For the calculation of the electronic structure, we take the offset of the conduction zone to be 440 meV, the applied electric field of K = 48 kV/cm, while the doping concentration N_s=4e15 m^{-2} per cascade. **b** Components of the dielectric permittivity tensor; in the isotropic model both components are equal to $\varepsilon_{||}$

4 Numerical results and discussion

We will now use our anisotropic model on the mid-IR GaAs/$Al_{0.45}Ga_{0.55}As$ QCL active region from (Atkins 2013) (#MR2784) and calculate eigenenergies and eigenfunctions using the transfer matrix method (TMM) (Vukovic et al. 2014; Vuković et al. 2014). The active region consists of three quantum wells and the injector region consists of five quantum wells. The expected transition is diagonal, the electron from the injector minizone will resonate with the third state of the active region (blue line in Fig. 1a) and will then dissipate into the second state of the active region (green line). Figure 1a shows only 3 states that are relevant for the lasing action. The eigenenergies are $E_1 = 144.4$ meV (red), $E_2 = 184.8$ meV (green), and $E_3 = 321$ meV (blue). The calculated wavelength of the lasing transition 3–2 is equal to $2\pi\hbar c/E_{32} = 9.122$ µm, close to the one reported in (Atkins 2013).

The resonant energy for LO phonon scattering is not only dependent on the material system used, but also on the layer structure itself, so it is of interest to find the contribution of the electronic structure. The angular frequency of the phonon transition $\tilde{\omega}_{LO}$ according to Eq. (4) depends on both the lateral and the normal components of the dielectric permittivity given by Eqs. (2) and (3) respectively. Figure 1b presents $\varepsilon_{||}$ (dashed) and $\varepsilon_{\perp}$ (full line). While $\varepsilon_{||}$ contains only the frequency mode which originates from the material itself (~36.5 meV), the normal permittivity component $\varepsilon_{\perp}$ depends in addition on the contributions from the three transitions: 2–1 (~40.4 meV), 3–2 (~136.2 meV) and 3–1 (~176.6 meV). Figure 1b shows that the contribution of 2–1 transition to $\varepsilon_{\perp}$ is dominant, the contribution of the transition 3–2 is also visible (although not very pronounced), while the contribution of the 3–1 transition is minor.

We numerically solve the Eq. (4) in the vicinity of the four frequencies (LO phonon modes) corresponding to material LO phonon energy and transition energies between the levels in Fig. 1a. Dispersion relations are shown in Fig. 2.

We now determine subband populations and scattering rates through the iterative procedure (as was explained in Sect. 2). The evolution of these quantities is shown in Table 1, and the results for the subband populations are also plotted in Fig. 3a. We observe that the

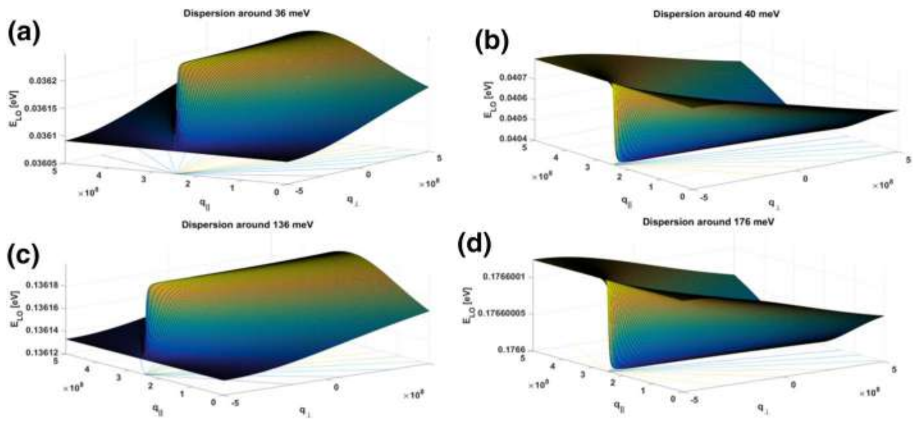

Fig. 2 Dependence of LO phonon energy on the phonon wavevector components $q_{\perp}$ and $q_{||}$ (dispersion). The four energies around which we numerically find zeros of the Eq. (4) correspond to **a** LO phonon energy of a given material, **b** transition 2–1, **c** transition 3–2, and **d** transition 3–1 in the active region of MR2784 (Atkins 2013)

Table 1 Anisotropic model of dielectric permittivity of the QCL active region- the evolution of electron sheet densities and scattering rates in each iteration of the self-consistent procedure until the algorithm converges

Iter. No	N_{s1} [m^{-2}]	N_{s2} [m^{-2}]	N_{s3} [m^{-2}]	W_{31} [s^{-1}]	W_{32} [s^{-1}]	W_{21} [s^{-1}]	W_{13} [s^{-1}]	W_{23} [s^{-1}]	W_{12} [s^{-1}]
1	$1.3333*10^{15}$	$1.3333*10^{15}$	$1.3333*10^{15}$	$1.3416*10^{11}$	$2.7908*10^{11}$	$2.8019*10^{12}$	0	$8.7060*10^{8}$	$6.0585*10^{11}$
				$7.5973*10^{11}$	$1.5946*10^{12}$	$1.6762*10^{13}$	0	$5.7766*10^{9}$	$3.5182*10^{12}$
				$3.6430*10^{14}$	$1.3602*10^{15}$	$3.2404*10^{13}$	$4.3823*10^{11}$	$7.0170*10^{12}$	$9.6418*10^{12}$
				$1.1725*10^{15}$	$3.7943*10^{14}$	0	$1.2667*10^{12}$	$1.7716*10^{12}$	$3.7315*10^{12}$
2	$3.0041*10^{15}$	$9.9150*10^{14}$	$4.4116*10^{12}$	$1.1881*10^{11}$	$2.8054*10^{11}$	$2.4168*10^{12}$	0	$8.4306*10^{8}$	$5.9565*10^{11}$
				$1.0402*10^{10}$	$4.4080*10^{10}$	$1.2430*10^{11}$	0	$1.5013*10^{8}$	$2.9428e*10^{10}$
				$2.7377*10^{9}$	$1.3775*10^{10}$	$5.9834*10^{8}$	$3.9113*10^{6}$	$7.5212*10^{7}$	$1.9532*10^{8}$
				$5.7860*10^{8}$	549.8105	0	$7.4656*10^{5}$	2.9931	$7.6409*10^{3}$
3	$2.0038*10^{15}$	$6.6932*10^{14}$	$1.3269*10^{15}$	$1.2730*10^{11}$	$2.8718*10^{11}$	$2.6256*10^{12}$	0	$8.2994*10^{8}$	$6.1426*10^{11}$
				$1.6498*10^{10}$	$6.4676*10^{10}$	$1.9591*10^{11}$	0	$2.1225*10^{8}$	$4.4476*10^{10}$
				$4.3779*10^{9}$	$2.1071*10^{10}$	$8.8396*10^{8}$	$5.5167*10^{6}$	$1.0449*10^{8}$	$2.9814*10^{8}$
				$6.2114*10^{8}$	586.1509	0	$6.9838*10^{5}$	2.7752	$7.7704*10^{3}$
4	$2.1437*10^{15}$	$6.5855*10^{14}$	$1.1978*10^{15}$	$1.2605*10^{11}$	$2.8706*10^{11}$	$2.5937*10^{12}$	0	$8.2872*10^{8}$	$6.1294*10^{11}$
				$1.4755*10^{10}$	$5.8913*10^{10}$	$1.7533*10^{11}$	0	$1.9300*10^{8}$	$4.0168*10^{10}$
				$5.2937*10^{9}$	$2.5697*10^{10}$	$1.0767*10^{9}$	$6.7821*10^{6}$	$1.2833*10^{8}$	$3.6375*10^{8}$
				$6.1607*10^{8}$	582.8361	0	$7.0387*10^{5}$	2.7959	$7.7761*10^{3}$
5	$2.1304*10^{15}$	$6.6404*10^{14}$	$1.2055*10^{15}$	$1.2617*10^{11}$	$2.8701*10^{11}$	$2.5969*10^{12}$	0	$8.2908*10^{8}$	$6.1296*10^{11}$
				$1.4949*10^{10}$	$5.9556*10^{10}$	$1.7762*10^{11}$	0	$1.9524*10^{8}$	$4.0646*10^{10}$
				$5.2758*10^{9}$	$2.5582*10^{10}$	$1.0726*10^{9}$	$6.7491*10^{6}$	$1.2773*10^{8}$	$3.6211*10^{8}$
				$6.1648*10^{8}$	582.9970	0	$7.0345*10^{5}$	2.7947	$7.7736*10^{3}$
6	$2.1327*10^{15}$	$6.6361*10^{14}$	$1.2037*10^{15}$	$1.2615*10^{11}$	$2.8701*10^{11}$	$2.5964*10^{12}$	0	$8.2905*10^{8}$	$6.1295*10^{11}$
				$1.4921*10^{10}$	$5.9463*10^{10}$	$1.7729 * 10^{11}$	0	$1.9492*10^{8}$	$4.0577*10^{10}$
				$5.2884e*10^{9}$	$2.5647*10^{10}$	$1.0753*10^{9}$	$6.7670*10^{6}$	$1.2807*10^{8}$	$3.6304*10^{8}$
				$6.1640*10^{8}$	582.9531	0	$7.0353*10^{5}$	2.7949	$7.7738*10^{3}$
7	$2.1324*10^{15}$	$6.6370*10^{14}$	$1.2039*10^{15}$	$1.2615*10^{11}$	$2.8701*10^{11}$	$2.5964*10^{12}$	0	$8.2905*10^{8}$	$6.1295*10^{11}$
				$1.4924*10^{10}$	$5.9474*10^{10}$	$1.7733*10^{11}$	0	$1.9496*10^{8}$	$4.0586*10^{10}$
				$5.2880*10^{9}$	$2.5645*10^{10}$	$1.0752*10^{9}$	$6.7663*10^{6}$	$1.2806*10^{8}$	$3.6300*10^{8}$
				$6.1641*10^{8}$	582.9562	0	$7.0352*10^{5}$	2.7949	$7.7738*10^{3}$

Table 1 (continued)

Iter. No	N_{s1} $[m^{-2}]$	N_{s2} $[m^{-2}]$	N_{s3} $[m^{-2}]$	W_{31} $[s^{-1}]$	W_{32} $[s^{-1}]$	W_{21} $[s^{-1}]$	W_{13} $[s^{-1}]$	W_{23} $[s^{-1}]$	W_{12} $[s^{-1}]$
8	$2.1325*10^{15}$	$6.6369*10^{14}$	$1.2038*10^{15}$	$1.2615*10^{11}$	$2.8701*10^{11}$	$2.5964*10^{12}$	0	$8.2905*10^{8}$	$6.1295*10^{11}$
				$1.4924*10^{10}$	$5.9472*10^{10}$	$1.7733*10^{11}$	0	$1.9496*10^{8}$	$4.0584*10^{10}$
				$5.2882*10^{9}$	$2.5646*10^{10}$	$1.0752*10^{9}$	$6.7666*10^{6}$	$1.2806*10^{8}$	$3.6302*10^{8}$
				$6.1641*10^{8}$	582.9555	0	$7.0352*10^{5}$	2.7949	$7.7738*10^{3}$
9	$2.1325*10^{15}$	$6.6369*10^{14}$	$1.2038*10^{15}$						

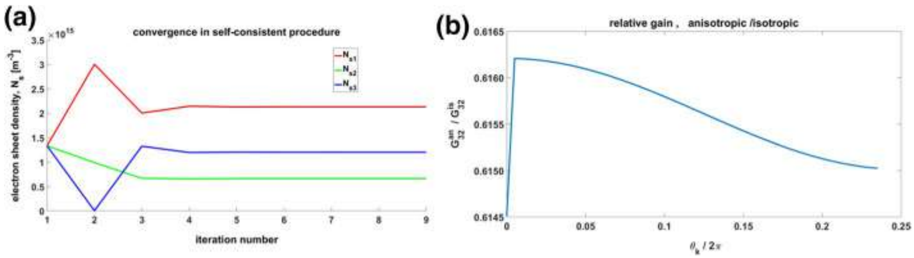

Fig. 3 **a** Evolution of electron sheet density through iterations and **b** gain ratio for the lasing transition 3–2 calculated using anisotropic model (given by Eq. (20)) and isotropic model, vs. angle θ_κ (introduced in Sect. 2)

algorithm converges after a few (8) iterations. Note that $N_{s,3} > N_{s,2}$ which is a prerequisite for the inverse population and thus positive gain. In addition, $N_{s,1} > N_{s,3}$ which is justified by the fact that we use a 3-level model from the system (16) and unit injection, and the carriers from level 1 (lowest level) need to be injected into the adjacent cascade of the structure. The four numerical values that are shown for each scattering rate in Table 1 represent the contribution of each of the LO phonon modes (from Fig. 2), and their sum represents the total scattering rate of that transition. For comparison we also display the results of the iterative procedure for the isotropic model of dielectric permittivity in Table 2. One may see from Table 2 that the self-consistent algorithm converges faster in the isotropic case, where for the calculation of W_{ij} we only considered a contribution from one LO-phonon mode (corresponding to a material, transition energy ~ 36 meV) shown in Fig. 2a. The final values of N_{si}, W_{ij} notably differ from values presented in Table 1.

The final calculated electron densities (output from the self-consistent procedure) are then used to find the optical gain for the lasing transition 3->2 and it is compared to the isotropic model predictions; see Fig. 3b. From Fig. 3b we see that the dependence of relative gain on θ_κ is nearly a constant, while there is a significant change of gain calculated from the anisotropic model compared to the gain calculated using the isotropic model (ratio of ~ 62%). This significant difference between the predictions of the two models originates mainly from the different final sheet carrier densities: the anisotropic model incorporates contributions of all four LO-phonon modes in the iterative procedure (see Tables 1 and 2, values of final N_{s3} and N_{s2}).

5 Summary

In this theoretical contribution, we have numerically elucidated that the anisotropy of the QCL active region dielectric permittivity has an important effect on the distribution of electrons between the subbands, consequently on electron-LO phonon scattering rates between the relevant states and the optical gain. We have demonstrated our claim on the example of the 3-well QCL active region reported in the literature. Future work will entail the inclusion of additional scattering mechanisms and impact on THz QCLs, confinement factor modifications due to anisotropy, modeling of left hand materials as well as the inclusion of an external magnetic field.

Table 2 Isotropic model of dielectric permittivity of the QCL active region- the evolution of electron sheet densities and scattering rates in each iteration of the self-consistent procedure until the algorithm converges

Iter. No	N_{s1} [m^{-2}]	N_{s2} [m^{-2}]	N_{s3} [m^{-2}]	W_{31} [s^{-1}]	W_{32} [s^{-1}]	W_{21} [s^{-1}]	W_{13} [s^{-1}]	W_{23} [s^{-1}]	W_{12} [s^{-1}]
1	$1.3333*10^{15}$	$1.3333*10^{15}$	$1.3333*10^{15}$	$1.3416*10^{11}$	$2.7908*10^{11}$	$2.8019*10^{12}$	0	$8.7060*10^{8}$	$6.0585*10^{11}$
2	$1.9224*10^{15}$	$5.6605*10^{14}$	$1.5116*10^{15}$	$1.2954*10^{11}$	$2.9195*10^{11}$	$2.7079*10^{12}$	0	$8.3319*10^{8}$	$6.3330*10^{11}$
3	$1.9114e*10^{15}$	$6.0661*10^{14}$	$1.4820*10^{15}$	$1.2962*10^{11}$	$2.9127*10^{11}$	$2.7091*10^{12}$	0	$8.3515e*10^{8}$	$6.3184*10^{11}$
4	$1.9108*10^{15}$	$6.0504*10^{14}$	$1.4841*10^{15}$	$1.2963*10^{11}$	$2.9129*10^{11}$	$2.7093*10^{12}$	0	$8.3507*10^{8}$	$6.3190*10^{11}$
5	$1.9109*10^{15}$	$6.0507*10^{14}$	$1.4840*10^{15}$	$1.2963*10^{11}$	$2.9129*10^{11}$	$2.7092*10^{12}$	0	$8.3507*10^{8}$	$6.3190*10^{11}$
6	$1.9109*10^{15}$	$6.0507*10^{14}$	$1.4840*10^{15}$						

Appendix A: Anisotropic gain expression

We assume the following spatial distribution of the magnetic field:

$$\underline{H}_y(x,z) = H_0 e^{i(\kappa_x x + \kappa_z z)}, H_0 \in \mathcal{R} \tag{23}$$

The total time-dependent magnetic field can be expressed as:

$$H_y(x,z,t) = \frac{H_y e^{-i\omega t} + \underline{H}_y{}^* e^{i\omega t}}{2} \tag{24}$$

From Maxwell equations, one can express x and z components of the electric field in terms of the magnetic field as:

$$\begin{aligned} \frac{\partial H_y}{\partial z} &= i\omega\varepsilon_\perp \varepsilon_0 \underline{E_x} \Rightarrow E_x = \frac{\kappa_z}{\omega\varepsilon_\perp \varepsilon_0} H_y \\ \frac{\partial \underline{H}_y}{\partial x} &= -i\omega\varepsilon_\| \varepsilon_0 E_z \Rightarrow E_z = \frac{-\kappa_x}{\omega\varepsilon_\| \varepsilon_0} \underline{H}_y \end{aligned} \tag{25}$$

The Pointing vector is given by:

$$\vec{S} = \vec{E} \times \vec{H} = E_x H_y \vec{\mathrm{i}}_z + E_z H_y \left(-\vec{i}_x\right) \tag{26}$$

The intensity of electromagnetic radiation will be found by averaging the Pointing vector during one period:

$$\begin{aligned} \overline{S_x} &= \overline{E_z H_y} = \frac{1}{2}\mathrm{Re}\left\{\underline{E_z}\underline{H_y}^*\right\} = \frac{1}{2}\mathrm{Re}\left\{\frac{\kappa_x}{\omega\varepsilon_\|\varepsilon_0} H_0^2\right\} = \frac{H_0^2}{2\omega\varepsilon_0\varepsilon_\|}\kappa_{x_R} = \frac{H_0^2}{2\omega\varepsilon_0\varepsilon_\|}|\kappa_R|\cos\left(\theta_\kappa\right) \\ \overline{S_z} &= \overline{E_x H_y} = \frac{H_0^2\kappa_z}{2\omega\varepsilon_0}\mathrm{Re}\left\{\frac{1}{\varepsilon_\perp}\right\} = \frac{H_0^2}{2\omega\varepsilon_0}\mathrm{Re}\left\{\frac{1}{\varepsilon_\perp}\right\}|\kappa_R|\sin\left(\theta_\kappa\right) \end{aligned} \tag{27}$$

The intensity is then found as:

$$I = |\vec{S}| = \sqrt{\left|S_x\right|^2 + \left|S_z\right|^2} = \frac{H_0^2|\kappa_R|}{2\omega\varepsilon_0}\sqrt{\frac{\cos^2\left(\theta_\kappa\right)}{\varepsilon_\|^2} + \left[\mathrm{Re}\left\{\frac{1}{\varepsilon_\perp}\right\}\right]^2 \sin^2\left(\theta_\kappa\right)} \tag{28}$$

We will express the amplitude of the magnetic field in terms of the electric one:

$$\left|E_{x_0}\right| = \left|\frac{\kappa_z}{\omega\varepsilon_\perp}\right|\frac{H_0}{\varepsilon_0} \tag{29}$$

$$\left|E_{z_0}\right| = \left|\frac{\kappa_x}{\omega\varepsilon_{||}}\right|\frac{H_0}{\varepsilon_0} \tag{30}$$

$$\left|E_0\right| = \sqrt{\left|E_{x_0}\right|^2 + \left|E_{z_0}\right|^2} = \frac{H_0}{\omega\varepsilon_0}\sqrt{\left|\frac{\kappa_z}{\varepsilon_\perp}\right|^2 + \left|\frac{\kappa_x}{\varepsilon_\parallel}\right|^2} \tag{31}$$

$$H_0{}^2 = \frac{\omega^2\varepsilon_0{}^2\left|E_0\right|^2}{\left|\frac{\kappa_z}{\varepsilon_\perp}\right|^2 + \left|\frac{\kappa_x}{\varepsilon_\parallel}\right|^2} = \frac{\omega^2\varepsilon_0{}^2\left|E_0\right|^2}{\left|\kappa_R\right|^2\left(\frac{\sin^2(\theta_\kappa)}{\left|\varepsilon_\perp\right|^2} + \frac{\cos^2(\theta_\kappa)}{\varepsilon_\parallel{}^2} + \left(\frac{\kappa_{xI}}{\kappa_R}\right)^2\frac{1}{\varepsilon_\parallel{}^2}\right)} \tag{32}$$

Now we finally get the intensity in the desired form:

$$I = I_0\frac{\kappa_0}{\left|\kappa_R\right|}\frac{1}{n_0}\left\{\frac{\sqrt{\frac{\cos^2(\theta_\kappa)}{\varepsilon_\parallel^2} + \left[\mathrm{Re}\left\{\frac{1}{\varepsilon_\perp}\right\}\right]^2\sin^2(\theta_\kappa)}}{\frac{\sin^2(\theta_\kappa)}{\left|\varepsilon_\perp\right|^2} + \frac{\cos^2(\theta_\kappa)}{\varepsilon_\parallel{}^2} + \left(\frac{\kappa_{xI}}{\kappa_R}\right)^2\frac{1}{\varepsilon_\parallel{}^2}}\right\} \tag{33}$$

where $I_0 = \frac{1}{2}\varepsilon_0 c\left|E_0\right|^2 n_0$ is the radiation intensity in the isotropic model ($\varepsilon = \varepsilon_\parallel$ in all directions), and $n_0 = \sqrt{\mathcal{E}_\parallel}$. The real part of the QCL refractive index is:

$$n_R^2 = \frac{\left|\kappa_R\right|^2}{\kappa_0^2} = \frac{\kappa_z^2 + \kappa_{x_R}^2}{\frac{\kappa_{x_R}^2}{\varepsilon_\parallel} + \mathrm{Re}\left\{\frac{1}{\varepsilon_\perp}\right\}\kappa_z^2} = \frac{1}{\frac{\cos^2(\theta_\kappa)}{\varepsilon_\parallel} + \mathrm{Re}\left\{\frac{1}{\varepsilon_\perp}\right\}\sin^2(\theta_\kappa)} \tag{34}$$

We will now address the correction of the matrix element:

$$\left|H_{if}^{'}\right|^2 = \frac{e^2}{m_0^2}\left|\int \Psi_f^*\vec{A}\vec{p}\Psi_i dV\right|^2 = \frac{e^2}{m_0^2}Q \tag{35}$$

where $\vec{A}$ and $\vec{p}$ are magnetic vector potential and momentum operators respectively. From the expression (35), the electric field vector reads:

$$\vec{E}(x,z,t) = \frac{1}{2}\left(\frac{\kappa_z}{\omega\varepsilon_\perp\varepsilon_0}\underline{H_y}\vec{i}_x - \frac{\kappa_x}{\omega\varepsilon_{||}\varepsilon_0}\underline{H_y}\vec{i}_z\right)e^{-i\omega t} \tag{36}$$

where complex conjugate terms have been neglected since they represent a spontaneous emission process. Magnetic vector potential then reads:

$$\vec{A} = -\int \vec{E}dt = \frac{H_0}{2i\omega^2\varepsilon_0}\left(\frac{\kappa_z}{\varepsilon_\perp}\vec{\mathrm{i}}_x - \frac{\kappa_x}{\varepsilon_\parallel}\vec{i}_z\right)e^{i(\kappa_x x + \kappa_z z - \omega t)} \tag{37}$$

We can now find the expression for the quantity Q from (35):

$$
\begin{aligned}
e^{i\omega t}\int \Psi_f^* \vec{A}\vec{p}\Psi_i dV &= \frac{H_0}{2\mathrm{i}\omega^2\varepsilon_0}\frac{\kappa_z}{\varepsilon_\perp}\int \Psi_f^* e^{i(\kappa_x x+\kappa_z z)}\hat{p}_x\Psi_i dV - \frac{H_0}{2\mathrm{i}\omega^2\varepsilon_0}\frac{\kappa_x}{\varepsilon_\parallel}\int \Psi_f^* e^{i(\kappa_x x+\kappa_z z)}\hat{p}_x\Psi_i dV \\
&= \frac{H_0}{2\mathrm{i}\omega^2\varepsilon_0}\left(\frac{\kappa_z}{\varepsilon_\perp}P_{i,f_x} - \frac{\kappa_x}{\varepsilon_\parallel}P_{i,f_z}\right) \\
Q = \left|\int \Psi_f^* \vec{A}\vec{p}\Psi_i dV\right|^2 &= \frac{H_0^2}{4\omega^4\varepsilon_0^2}\left|\frac{\kappa_z}{\varepsilon_\perp}P_{i,f_x} - \frac{\kappa_x}{\varepsilon_\parallel}P_{i,f_z}\right|^2 \\
&= \frac{H_0^2}{4\omega^4\varepsilon_0^2}\left(\frac{|\kappa_z|^2}{|\varepsilon_\perp|^2}\left|P_{i,f_x}\right|^2 - \frac{\kappa_z}{\varepsilon_\perp}P_{i,f_x}\frac{\kappa_x^*}{\varepsilon_\parallel^*}P_{i,f_z}^* - \frac{\kappa_x}{\varepsilon_\parallel}P_{i,f_z}\frac{\kappa_z^*}{\varepsilon_\perp^*}P_{i,f_x}^* + \frac{|\kappa_x|^2}{|\varepsilon_\parallel|^2}\left|P_{i,f_z}\right|^2\right) \\
Q &= \frac{H_0^2}{4\omega^4\varepsilon_0^2}\left(\frac{|\kappa_z|^2}{|\varepsilon_\perp|^2}\left|P_{i,f_x}\right|^2 + \frac{|\kappa_x|^2}{|\varepsilon_\parallel|^2}\left|P_{i,f_z}\right|^2 - 2\mathrm{Re}\left\{\frac{\kappa_z}{\varepsilon_\perp}P_{i,f_x}\frac{\kappa_x^*}{\varepsilon_\parallel^*}P_{i,f_z}^*\right\}\right) \\
&= \frac{H_0^2|\kappa_R|^2}{4\omega^4\varepsilon_0^2|\varepsilon_\perp|^2}\left(\left|P_{i,f_x}\right|^2\sin^2(\theta_\kappa) + \frac{|\varepsilon_\perp|^2}{\varepsilon_\parallel^2}\left|P_{i,f_z}\right|^2\left(\cos^2(\theta_\kappa) + \left|\frac{\kappa_{xI}}{\kappa_R}\right|^2\right) - 2\mathrm{Re}\left\{\frac{\kappa_z}{|\kappa_R|^2\varepsilon_\perp}P_{i,f_x}\frac{\kappa_x^*}{\varepsilon_\parallel^*}P_{i,f_z}^*\right\}\right)
\end{aligned}
\tag{38}
$$

From Eq. (32) we can express ${H_0}^2|\kappa_R|^2$ and insert in (38) to find:

$$
\mathrm{Q} = \frac{|E_0|^2}{4\omega^2|\varepsilon_\perp|^2}\frac{\left(\left|P_{i,f_x}\right|^2\sin^2(\theta_\kappa) + \frac{|\varepsilon_\perp|^2}{{\varepsilon_\parallel}^2}\left|P_{i,f_z}\right|^2\left(\cos^2(\theta_\kappa) + \left|\frac{\kappa_{xI}}{\kappa_R}\right|^2\right) - 2\mathrm{Re}\left\{\frac{\kappa_z}{|\kappa_R|^2\varepsilon_\perp}P_{i,f_x}\frac{{\kappa_x}^*}{{\varepsilon_\parallel}^*}P_{i,f_z}^*\right\}\right)}{\left(\frac{\sin^2(\theta_\kappa)}{|\varepsilon_\perp|^2} + \frac{\cos^2(\theta_\kappa)}{\varepsilon_\parallel^2} + \left(\frac{\kappa_{xI}}{\kappa_R}\right)^2\frac{1}{\varepsilon_\parallel^2}\right)}
\tag{39}
$$

Using Eqs. (33), (35), and (39) we get:

$$
\frac{\left|H_{if}'\right|^2}{I} = \frac{e^2}{m_0^2}\frac{n_R}{2\omega^2\varepsilon_0 c|\mathcal{E}_\perp|^2}\frac{\left|P_{i,f_x}\right|^2\sin^2(\theta_\kappa) + \frac{|\varepsilon_\perp|^2}{{\varepsilon_\parallel}^2}\left|P_{i,f_z}\right|^2\left(\cos^2(\theta_\kappa) + \left|\frac{\kappa_{xI}}{\kappa_R}\right|^2\right) - 2\mathrm{Re}\left\{\frac{\kappa_z}{|\kappa_R|^2\varepsilon_\perp}P_{i,f_x}\frac{{\kappa_x}^*}{{\varepsilon_\parallel}^*}P_{i,f_z}^*\right\}}{\sqrt{\frac{\cos^2(\theta_\kappa)}{\varepsilon_\parallel^2} + \left[\mathrm{Re}\left\{\frac{1}{\varepsilon_\perp}\right\}\right]^2\sin^2(\theta_\kappa)}}
\tag{40}
$$

QCL gain with the anisotropic active region can now be expressed as:

$$
G_{if} = \frac{e^2\omega Q}{{m_0}^2 I}L(\hbar\omega)2\pi\left(N_{s_i} - N_{s_f}\right)
\tag{41}
$$

which after applying (40) brings us to the final result:

$$
G_{if} = \frac{e^2\pi n_R L(\hbar\omega)}{m_0^2\omega\varepsilon_0 c|\varepsilon_\perp|^2}\frac{\left|P_{i,f_x}\right|^2\sin^2(\theta_\kappa) + \frac{|\varepsilon_\perp|^2}{{\varepsilon_\parallel}^2}\left|P_{i,f_z}\right|^2\left(\cos^2(\theta_\kappa) + \left|\frac{\kappa_{xI}}{\kappa_R}\right|^2\right) - 2\mathrm{Re}\left\{\frac{\kappa_z}{|\kappa_R|^2\varepsilon_\perp}P_{i,f_x}\frac{{\kappa_x}^*}{{\varepsilon_\parallel}^*}P_{i,f_z}^*\right\}}{\sqrt{\frac{\cos^2(\theta_\kappa)}{\varepsilon_\parallel^2} + \left[\mathrm{Re}\left\{\frac{1}{\varepsilon_\perp}\right\}\right]^2\sin^2(\theta_\kappa)}}\left(N_{s,i} - N_{s,f}\right)
\tag{42}
$$

Author's contributions All authors contributed to the study conception and design. Material preparation, data collection and analysis were performed by all authors. The first draft of the manuscript was written by Nikola Vukovic and all the authors contributed in finalizing the previous versions of the manuscript. All authors read and approved the submitted version of the manuscript.

Funding This work was supported by Ministry of Education, Science and Technological Development (Republic of Serbia); "Multi-Scale Modeling of Terahertz Quantum Cascade Laser Active Regions", Multilateral scientific and technological cooperation in the Danube region 2020–2021 (Grant Number

337–00-00322/2019–09/221); and "DEMETRA: Development of high-performance mid-IR/THz quantum cascade lasers for advanced applications", Science Fund of the Republic of Serbia, Serbian Science and Diaspora Collaboration Programme: Knowledge Exchange Vouchers (Grant Number 6436915).

Declarations

Conflict of interest The authors have no relevant financial or non-financial interests to disclose.

References

Atkins, C.N.: New developments in GaAs-based quantum cascade lasers. In: PhD thesis, University of Sheffield. pp. 1–125 (2013)

Baird, C.S.: Quantum cascade laser theory: phonon scattering. In: wtamu.edu/~cbaird. Univerisity of Massachusetts Lowell (2009)

Basu, P.K.: Theory of Optical Processes in Semiconductors. Oxford University Press, Oxford (2003)

Dubajić, M., Daničić, A., Vuković, N., Milanović, V., Radovanović, J.: Optimization of cubic GaN/AlGaN quantum cascade structures for negative refraction in the THz spectral range. Opt. Quantum Electron. **50**, 373 (2018). https://doi.org/10.1007/s11082-018-1639-1

Faist, J.: Quantum Cascade Lasers. OUP Oxford, Oxford (2013)

Faist, J., Capasso, F., Sivco, D.L., Sirtori, C., Hutchinson, A.L., Cho, A.Y.: Quantum cascade laser. Science (80-). **264**, 553–556 (1994). https://doi.org/10.1126/science.264.5158.553

Fuchs, F., Hugger, S., Kinzer, M., Aidam, R., Bronner, W., Lösch, R., Yang, Q., Degreif, K., Schnürer, F.: Imaging standoff detection of explosives using widely tunable midinfrared quantum cascade lasers. Opt. Eng. **49**, 111127 (2010). https://doi.org/10.1117/1.3506195

Ginzburg, P., Orenstein, M.: Metal-free quantum-based metamaterial for surface plasmon polariton guiding with amplification. J. Appl. Phys. **104**, 063513 (2008). https://doi.org/10.1063/1.2978208

Harrison, P., Valavanis, A.: Quantum Wells, Wires and Dots. Wiley, Chichester (2016)

Hugi, A., Villares, G., Blaser, S., Liu, H.C., Faist, J.: Mid-infrared frequency comb based on a quantum cascade laser. Nature **492**, 229–233 (2012). https://doi.org/10.1038/nature11620

Jirauschek, C., Kubis, T.: Modeling techniques for quantum cascade lasers. Appl. Phys. Rev. **1**, 011307 (2014). https://doi.org/10.1063/1.4863665

Ko, Y.H., Yu, J.S.: Design optimization of quantum cascade laser structures at λ ~ 11–12 μm. Phys. Status Solidi. **207**, 2190–2197 (2010). https://doi.org/10.1002/pssa.200925447

Li, J.S., Yu, B., Fischer, H., Chen, W., Yalin, A.P.: Contributed review: quantum cascade laser based photoacoustic detection of explosives. Rev. Sci. Instrum. **86**, 031501 (2015). https://doi.org/10.1063/1.4916105

Lyu, M., Gmachl, C.: Correction to the effective refractive index and the confinement factor in waveguide modeling for quantum cascade lasers. OSA Contin. **4**, 2275 (2021). https://doi.org/10.1364/OSAC.431383

Mueller, D., Triplett, G.: Development of a multi-objective evolutionary algorithm for strain-enhanced quantum cascade lasers. Photonics. **3**, 44 (2016). https://doi.org/10.3390/photonics3030044

Opačak, N., Schwarz, B.: Theory of frequency-modulated combs in lasers with spatial hole burning, dispersion, and kerr nonlinearity. Phys. Rev. Lett. (2019). https://doi.org/10.1103/PhysRevLett.123.243902

Ostendorf, R., Butschek, L., Hugger, S., Fuchs, F., Yang, Q., Jarvis, J., Schilling, C., Rattunde, M., Merten, A., Grahmann, J., Boskovic, D., Tybussek, T., Rieblinger, K., Wagner, J.: Recent advances and applications of external cavity-QCLs towards hyperspectral imaging for standoff detection and real-time spectroscopic sensing of chemicals. Photonics **3**, 28 (2016). https://doi.org/10.3390/photonics3020028

Radovanović, J., Vuković, N., Milanović, V.: Global optimization methods for the design of MIR-THz QCLs applied to explosives detection. In: NATO Science for Peace and Security Series B: Physics and Biophysics. pp. 71–86 (2021)

Sharma, R.C.: Standoff quantum cascade laser photoacoustic spectroscopy based explosive detection system. J. Lasers Opt. Photon. (2014). https://doi.org/10.4172/2469-410X.1000109

Singleton, M., Beck, M., Faist, J.: Pulses from a mid-infrared quantum cascade laser frequency comb using an external compressor. J. Opt. Soc. Am. b. (2019). https://doi.org/10.1364/josab.36.001676

Smiljanić, J., Žeželj, M., Milanović, V., Radovanović, J., Stanković, I.: MATLAB-based program for optimization of quantum cascade laser active region parameters and calculation of output characteristics in magnetic field. Comput. Phys. Commun. **185**, 998–1006 (2014). https://doi.org/10.1016/j.cpc.2013.10.025

Stroscio, M.A., Dutta, M.: Phonons in nanostructures. In: Phonons in nanostructures. pp. 1–5. Cambridge University Press (2001)

Villares, G., Hugi, A., Blaser, S., Faist, J.: Dual-comb spectroscopy based on quantum-cascade-laser frequency combs. Nat. Commun. **5**, 1–3 (2014). https://doi.org/10.1038/ncomms6192

Vitiello, M.S., Scalari, G., Williams, B., De Natale, P.: Quantum cascade lasers: 20 years of challenges. Opt. Express. (2015). https://doi.org/10.1364/OE.23.005167

Vuković, N., Daničić, A., Radovanović, J., Milanović, V., Indjin, D.: Possibilities of achieving negative refraction in QCL-based semiconductor metamaterials in the THz spectral range. Opt. Quantum Electron. **47**, 883–891 (2015). https://doi.org/10.1007/s11082-014-0020-2

Vuković, N., Milanović, V., Radovanović, J.: Influence of nonparabolicity on electronic structure of quantum cascade laser. Phys. Lett. A **378**, 2222–2225 (2014). https://doi.org/10.1016/j.physleta.2014.04.069

Vukovic, N., Radovanovic, J., Milanovic, V.: Enhanced modeling of band nonparabolicity with application to a mid-IR quantum cascade laser structure. Phys. Scr. **T162**, 014014 (2014). https://doi.org/10.1088/0031-8949/2014/T162/014014

Vukovic, N.N., Radovanovic, J., Milanovic, V., Boiko, D.L.: Low-threshold RNGH instabilities in quantum cascade lasers. IEEE J. Sel. Top. Quantum Electron. **23**, 1–16 (2017). https://doi.org/10.1109/JSTQE.2017.2699139

Wacker, A.: Quantum cascade laser: an emerging technology. In: Nonlinear laser dynamics, Berlin (2012)

Waldmueller, I., Wanke, M.C., Lerttamrab, M., Allen, D.G., Chow, W.W.: Inverse-quantum-engineering: a new methodology for designing quantum cascade lasers. IEEE J. Quantum Electron. (2010). https://doi.org/10.1109/JQE.2010.2049253

Williams, B.S.: Terahertz quantum-cascade lasers. Nat. Photon. **1**, 517–525 (2007). https://doi.org/10.1038/nphoton.2007.166